arXiv:1403.7513v1 [physics.optics] 28 Mar 2014

Localized lasing modes of triangular organic microlasers

C. Lafargue,[1] M. Lebental,[1] A. Grigis,[2] C. Ulysse,[3] I. Gozhyk,[1] N. Djellali,[1] J. Zyss,[1] and S. Bittner[1]

[1]*Laboratoire de Photonique Quantique et Moléculaire, CNRS UMR 8537, Institut d'Alembert FR 3242, École Normale Supérieure de Cachan, F-94235 Cachan, France*

[2]*Laboratoire Analyse, Géométrie et Applications, Université Paris 13, Sorbonne-Paris-Cité, LAGA, UMR-CNRS 7539, 99 avenue J. B. Clément, F-93430 Villetaneuse*

[3]*Laboratoire de Photonique et Nanostructures, CNRS UPR20, Route de Nozay, F-91460 Marcoussis, France*

(Dated: March 31, 2014)

We investigated experimentally the ray-wave correspondence in organic microlasers of various triangular shapes. Triangular billiards are of interest since they are the simplest cases of polygonal billiards and the existence and properties of periodic orbits in general triangles are not yet fully understood. The microlasers with symmetric shapes that were investigated exhibited states localized on simple periodic orbits, and almost all of their lasing characteristics like spectra and far-field distributions could be well explained by simple ray-optical calculations. Furthermore, asymmetric triangles that do not feature simple periodic orbits were studied. The modes of these microlasers were not localized on classical periodic orbits as for the symmetric triangles, but instead seem to be related to diffractive orbits.

PACS numbers: 05.45.Mt, 42.55.Sa, 03.65.Sq

INTRODUCTION

Two-dimensional (2D) billiards have been intensely studied as model systems with Hamiltonian dynamics for a long time. This is in great part due to their seeming simplicity that contrasts the wealth of different dynamical behaviors that they can exhibit, including integrable, chaotic, pseudo-integrable or mixed dynamics. One interesting class of 2D billiards are polygons, of which the triangles are the simplest case. While some classes of triangular billiards are well understood, many unsolved questions remain for triangles of general, asymmetric shape. These concern for example the existence, number, and stability with respect to geometric perturbations of periodic orbits (POs) of such triangular billiards [1–7]. For example, it is not even known whether any PO exists in asymmetric billiards with one angle greater than 100°. But even in the cases of triangles for which the existence of POs is assured, the actual construction of the POs is often nontrivial, and even the shortest POs can be very complicated.

Two-dimensional billiards are, however, more than just simple model systems. They are studied both theoretically and experimentally in the context of quantum and wave-dynamical chaos [8, 9] to understand the manifestation of classical (ray) dynamics in the properties of the corresponding quantum (wave-dynamical) systems. Early experiments concentrated on microwave and acoustic resonators [10–13], and new interest has arisen with the advent of applications like optical microcavities and -lasers [14, 15]. In particular the influence of classical POs on the spectral and emission properties of microlasers is important in view both of a fundamental understanding of these devices and their possible applications [16–19].

While many microcavities have circular or deformed circular shape, also different types of polygonal microresonators have been investigated. Examples of such structures include semiconductor [20, 21], organic [19, 22] and crystal microlasers [23], silicon and silica microresonators [24–26], VCSELs [27–30], and hexagonal zinc oxide nanocavities and -rods [31–33]. These studies, however, concern only equilateral polygons, while very few experimental investigations of nonequilateral polygonal resonators have been reported [34, 35]. Therefore the properties of nonequilateral triangular and polygonal microcavities are little understood. In this article, the lasing characteristics of triangular organic microlasers with varying shapes and degrees of symmetry are studied. Organic microlasers were used because their fabrication is simple, cheap, and rapid, and almost arbitrary shapes can be produced with high precision.

Our investigations focus on the manifestation of the POs of the corresponding classical billiards in the different experimental observables. We identify the POs that the lasing modes are localized on and try to understand the parameters that determine which out of several possible POs supports the dominant lasing modes. In the cases of symmetric triangles, the lasing modes were supported by families of relatively simple POs, though for some examples we also found indications of the influence of isolated POs. Several microlasers exhibited competing families of modes localized on different POs. Furthermore, two cases of asymmetric triangles were investigated that are of particular interest since the POs of the corresponding billiards are not evident. The modes of these microlasers were not localized on classical POs, but instead appeared to be related to diffractive POs.

The article is organized as follows. Section summa-

rizes the key characteristics of classical triangular billiards and their POs, and Sec. treats their implications in dielectric resonators. Section explains the fabrication of the microlasers and the experimental setup for their characterization. The experimental results for different triangular microlasers are presented in Sec. , starting with simple and well understood cases and finishing with completely asymmetric cavities. Section concludes with a summary and an outlook.

CLASSICAL DYNAMICS OF TRIANGULAR BILLIARDS

Triangles are the simplest type of polygons and can hence serve in many respects as paradigms of general polygons. The dynamics of a classical polygonal billiard with M vertices depends on the internal angles α_j at the vertices where $j = 1 \dots M$ is the index of the vertex. A polygonal billiard is called rational if all of its angles can be written as a rational multiple of π, that is, $\alpha_j = m_j\pi/n_j$, where the m_j and n_j are coprime integer numbers. All other polygons are called irrational. The topology of the phase space of a rational polygon is determined by its genus [36]

$$g = 1 + \frac{N}{2}\sum_{j=1}^{M}\frac{m_j - 1}{n_j} \tag{1}$$

where N is the least common multiple of the n_j. For $g = 1$ the phase space has the topology of a torus and the billiard is integrable. The three cases of integrable triangle billiards are the equilateral triangle, the right isosceles triangle (i.e., a square cut in half along the diagonal), and the triangle with angles $\pi/2$, $\pi/3$ and $\pi/6$ which is an equilateral triangle cut in half [5]. Microlasers with the first two of these geometries were investigated and are presented below. For $g > 1$, the phase space resembles a g-handled sphere and its dynamics are said to be pseudo-integrable [36]. Irrational polygons have ergodic dynamics [37].

One type of trajectories that plays an important role in the dynamics of both classical and wave-dynamical billiards are periodic orbits, that is, orbits that retrace themselves after finite time. One such example is shown in Fig. 1. While it has been proven that POs exist in any billiard with a smooth (C^1) contour [38], there is no such theorem for general polygonal billiards. There are, however, several results for specific cases. One of the oldest concerns acute triangles. It was proven already in the 18th century by Fagano that the PO connecting the feet of the three altitudes (see Fig. 1) is the shortest of all possible POs in such triangles [3]. It is hence called Fagano's orbit. The existence of other POs in irrational acute triangles is, however, not evident. The POs in rational triangles can be obtained with a different kind of geometric

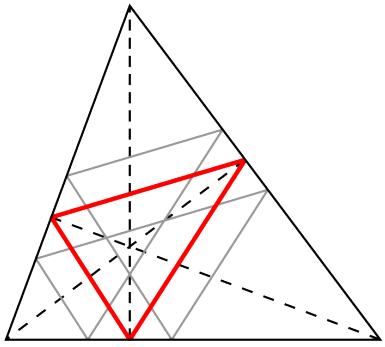

FIG. 1. Fagano's orbit in an acute triangle. The orbit (thick red line) connects the feet of the altitudes (dashed black lines). A trajectory parallel to Fagano's orbit but starting at a different position closes after two roundtrips (thin gray line).

construction, the so-called unfolding technique. This is demontsrated in Fig. 2(a) for an isosceles triangle with top angle 110°. We follow a trajectory (red line) that start perpendicularly to the height of the triangle by reflecting the triangle and continuing the trajectory in a straight line each time that it hits a side wall. The trajectory finally arrives again at its starting point after a finite number of reflections. The actual PO is obtained by folding the red line back into the triangle as demonstrated in Fig. 2(b). There are furthermore estimates for the number of POs up to a given length in rational triangles, and it has been shown that the POs are dense in the phase space [4]. One particular class of rational triangles for which even stronger theorems on the POs are known are the so-called Veech triangles [1, 5, 39]. Much less is known for irrational triangles. The POs in right and isosceles triangles can also be constructed by unfolding [2], and furthermore the existence of POs in triangles with all angles smaller than 100° has been proven [6]. However, no general statements are known for obtuse triangles with one angle larger than 100°. It should furthermore be noted that even in cases where POs can be constructed with the unfolding technique, the shortest PO can be long and complicated compared to the simple examples shown in Figs. 1 and 2.

All trajectories in polygonal billiards are marginally stable with respect to perturbations of their initial conditions. POs with an odd number of reflections like Fagano's orbit or the red PO in Fig. 2 are isolated, while POs with an even number of reflections are part of a family of POs with parallel trajectories [40, 41]. This includes in particular the repetitions of isolated POs as demonstrated by the PO indicated as gray line in Fig. 1. For rational triangles, the complete family of a PO can be easily found by means of unfolding since they cover a strip parallel to the PO. This strip is also called PO channel. The PO channel of the double-bowtie orbit in the isosceles 110° billiard is indicated in gray in Fig. 2. Note

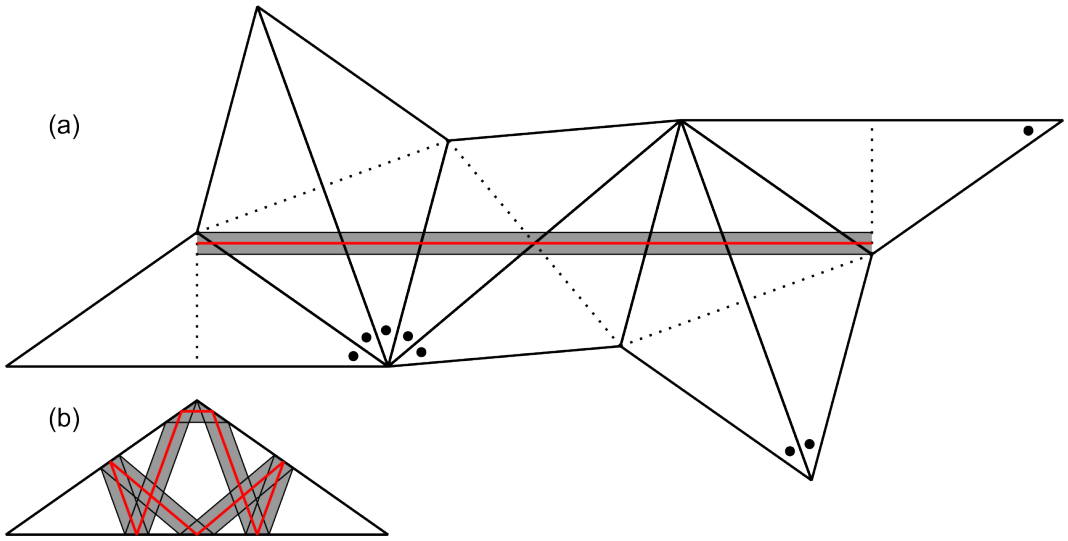

FIG. 2. Double-bowtie orbit in the isosceles triangle with top angle 110° unfolded (a) and folded back into a single triangle (b). The red line indicates the isolated PO at the center of the PO channel (gray) that is restricted by the thin black line touching the top corner of the triangle. The dotted black lines indicate the heigth of the triangle and the black dots indicate the orientation of the triangle.

that the POs in this channel have twice the period of the red PO since it has an odd number of reflections. The PO channel is bounded by two trajectories (thin black lines) that touch the corners of the triangle. These lines are also called optical boundaries. Parallel trajectories beyond these line are not members of that family as can be easily verified by unfolding them. Depending on the type of the PO, the PO channel can either cover a part of the billiard like in Fig. 2 or the complete billiard. The latter is the case for, e.g., the POs of the equilateral and right isosceles triangles since these triangles tesselate the plane when unfolding the POs.

DIELECTRIC RESONATORS AND PERIODIC ORBITS

The flat organic microlasers studied in this article are treated as 2D open dielectric resonators [19]. They are described by the scalar Helmholtz equation

$$[\Delta + n(x,y)^2 k^2]\Psi(x,y) = 0 \qquad (2)$$

where k is the free-space wave number and $n(x,y)$ is the effective refractive index n_{eff} for (x,y) inside the resonator domain and the refractive index of the surrounding medium, air with $n = 1$, otherwise. The wave function Ψ corresponds either to the electric field E_z for transverse magnetic (TM) modes or the magnetic field B_z for transverse electric (TE) modes. The wave functions inside and outside of the resonator are connected by the appropriate boundary conditions for dielectric interfaces.

Since the typical size of the cavities treated here is in the range of several hundred wavelengths, the resonators belong to the so-called semiclassical regime that is the transition regime from classical physics or ray optics to quantum mechanics or wave optics. Semiclassical methods allow for approximate descriptions of the resonators in terms of the dynamics of the corresponding classical billiard systems [41]. The POs play a particularly important role in these approximations. Examples are trace formulas connecting the density of state with the POs [41–43] and the observation of resonant states localized on POs, so-called scars [44] and superscars [45, 46]. The above mentioned examples focus on closed resonators with Dirichlet boundary conditions, but the underlying principles can be extended to dielectric resonators even though their openness adds complexity. In fact, a trace formula for dielectric resonators has been developed [22, 47–49], and modes of dielectric resonators localized on classical trajectories are often observed. This includes Gaussian modes that are localized on stable POs [16, 50], scar states localized on unstable POs [17, 18], and superscar states localized on families of marginally stable POs [19, 51] or classical tori [52]. It has been shown in Ref. [53] for resonators with Dirichlet boundary conditions that superscar states are localized inside the PO channel (see Fig. 2) due to repeated diffraction at the corners that define the optical boundaries. A similar effect has been proposed in Ref. [19] for dielectric resonators even though the diffraction at dielectric corners is not understood [54]. Therefore we expect the formation of superscarred lasing modes in triangular dielectric resonators with pseudo-integrable classical dynamics.

The influence of POs on the properties of closed resonators depends on several factors, among them the length and stability of the PO and, in the case of non-isolated orbits, the area covered by its family [41, 55]. Often the dominant contributions stem from a handful of the shortest POs. For dielectric resonators, another key factor is the refractive index. A ray inside a dielectric resonator is reflected and refracted at the side walls according to Snell's law and the Fresnel formulas. Therefore, the angles of incidence of a PO and the refractive index will determine the emission directions of the refracted rays and its losses. The dominant modes of passive dielectric cavities hence mainly exhibit the influence of the most well-confined POs [49]. On the other hand, also modes based on POs that are not confined by total internal reflections can be observed for laser cavities. The threshold gain g_{th} for a ray travelling along a PO with length ℓ_{geo} in an active medium is given by

$$g_{th} = -\frac{1}{\ell_{\text{geo}}} \sum_j \ln\{|r(\beta_j)|\} \tag{3}$$

where $r(\beta_j)$ is the Fresnel reflection coefficient for the reflection with angle of incidence β_j and the appropriate polarization and the sum runs over all vertices j of the PO. We use Eq. (3) as a simple estimate for the threshold of a mode localized on a PO. In practice, however, also other parameters like the overlap between the gain region and the mode profiles [56] or the coupling between the gain medium and different modes [57] can be of importance. The aim of the work presented here is to verify the existence of modes localized on POs in triangular microlasers, study the properties of these modes, and understand the different parameters that determine which POs supports the dominant lasing modes. The expermental techniques that were used for this are described in the next section.

It should furthermore be noted that even though the POs of a classical billiard can explain many properties of the corresponding resonators, also wave effects like tunneling and diffraction that are unknown to ray optics can have a significant influence. One example are so-called diffractive orbits that have one vertex at a diffractive corner of the billiard. Diffractive corners are corners with an angle that is not equal to π/m where m is an integer. The reflection of a ray at a diffractive corner is not defined, and hence diffractive oribts do not exist in classical mechanics. On the other hand, a wave impinging on such a corner is diffracted into various directions. This leads to contributions from diffractive POs for example in the trace formulas for closed resonators [58, 59]. Another important point is that the dynamics of wave systems is less prone to geometrical perturbations than classical systems. Therefore, the influence of POs on a wave system can survive geometrical perturbations even though the perturbation completely suppresses them in the classical dynamics [60, 61]. It is hence interesting to study which properties of the triangular microlasers can be explained by ray dynamics alone and which effects are beyond such simple approximations.

EXPERIMENTAL TECHNIQUES

The organic microlasers studied here consist of PMMA [Poly(methyl methacrylate)] doped with 5 wt% of the laser dye DCM[1]. A solution of PMMA and DCM is spin-coated on a silicon wafer with a 2 μm thick layer of silica. The thickness of the PMMA layer is about 700 nm. After baking the polymer film, the desired cavity shapes are written by 100 kV electron-beam lithography. This process allows to define the cavity boundaries with nanometric precision and achieve vertical side walls and sharp corners and edges [62]. The triangular microlasers considered here have typical side lengths a in the range of 200 μm to 400 μm, i.e., several hundred times larger than the wavelength $\lambda \approx 600$ nm. They are considered as 2D systems with an effective refractive index of $n_{\text{eff}} = 1.50$ since they are only about one wavelength thick and support only a single vertical excitation for each polarization [19].

The experimental setup is similar to the one described in Ref. [63]. The microlasers are pumped by a pulsed frequency-doubled Nd:YAG laser (532 nm, 500 ps, 10 Hz) that impinges perpendicularly to the cavity plane. The intensity and the polarization of the pump beam are controlled independently using half- and quarter-wavelength plates and polarizers. A circularly polarized pump beam was used throughout this article. The diameter of the pump beam was adjusted to cover the complete area of a single microlaser. The lasing emission in the plane of the microlasers is collected in the far-field by a lens 18 cm away from the sample and transferred to a spectrometer (Spectra Pro 2500i, Acton Research) and a cooled CCD camera via a fiber. The samples can be rotated so that the spectra in each direction in the plane of the cavity can be recorded. This is used to measure the azimuthal far-field distributions. The polarization of the lasing emission is determined using a polarization filter [57]. Furthermore, a CMOS sensor camera (UI324xCP-C, IDS Imaging) with a zoom lens (Zoom 6000, Navitar) was used to take photographs of the lasing cavities. The observation angle of the camera was chosen slightly out of the plane so that the whole cavity could be surveyed.

Various properties of the lasing modes, and thus the POs that they might be localized on, can be deduced from the experimental observables. The main observ-

[1] 4-(Dicyanomethylene)-2-methyl-6-(4-dimethylaminostyryl)-4H-pyran (by Exciton)

ables are the lasing thresholds, spectra, azimuthal far-field distributions, and photos taken with the camera. It should be noted, however, that not all lasing modes are in fact localized on specific classical trajectories. Therefore, a careful analysis of all available data is needed to decide the nature of the observed resonant states. The lasing thresholds are related to the lifetime of the cavity modes and hence to the losses of a possible underlying PO [cf. Eq. (3)]. The far-field distributions are often concentrated around a few specific directions. From these directions one can deduce the trajectories that the lasing modes are based on via Snell's law. The photographs show the points of origin of the lasing emission. The spectra typically exhibit multimode lasing with several tens of resonances. They are often organized in combs of equidistant resonances. If a set of lasing modes is localized on a specific PO or family of POs, the optical length $\ell_{\rm opt}$ of this PO can be deduced from the free spectral range (FSR), $\lambda_{\rm FSR}$, via the relation

$$\ell_{\rm opt} = \frac{\lambda^2}{\lambda_{\rm FSR}} \tag{4}$$

where λ is the wavelength of the lasing emission [19]. The optical length can be conveniently obtained from the Fourier transform (FT) of the spectrum that will feature peaks at $\ell_{\rm opt}$ and its multiples. The geometrical length of the PO, $\ell_{\rm geo}$, is related to the optical length via $\ell_{\rm opt} = n_g \ell_{\rm geo}$ where n_g is the group refractive index. The latter is different from the effective refractive index since it also takes into account dispersion [19]. It has a value in the range of $n_g = 1.60$ to 1.64 depending on the sample considered. The precise value for each sample can be determined from calibration measurements with ribbon-shaped Fabry-Pérot cavities since these feature only a single type of PO [19].

EXPERIMENTAL RESULTS

Equilateral triangle (ET)

The equilateral triangle (ET) is the triangle with the highest degree of symmetry, and microlasers with equilateral triangular shape have been intensely studied [20, 21, 27–30, 64–69]. The equilateral triangle billiard is an integrable system, and the corresponding resonator problem with Dirichlet or Neumann boundary conditions can be solved analytically [41]. This problem was already investigated in the context of vibrating membranes by Lamé in the 19th century [70]. There is, however, no analytical solution in the case of dielectric boundary conditions considered here. All POs of the ET are known, but none of them is confined by total internal reflection (TIR) at all its reflections. This is due to the relatively low value of $n = 1.5$ that corresponds to a critical angle of $\alpha_{\rm crit} = \arcsin(1/n) \approx 42°$. The lack of good confinement necessitated a large microlaser with a side length of $a = 300$ μm to provide sufficient gain. This applies also to all the other triangular microlasers considered here.

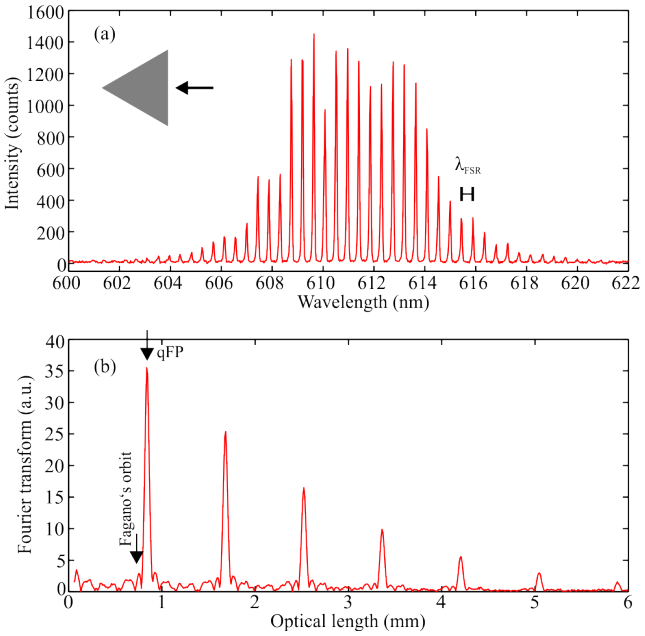

FIG. 3. (a) Spectrum of the ET microlaser in the direction $\varphi = 0°$ (as indicated in the inset). (b) Fourier transform of the spectrum shown in (a). The two arrows indicate the optical lengths of Fagano's orbit and the quasi-Fabry-Pérot orbits, respectively.

Figure 3(a) shows the lasing spectrum $I(\lambda)$ of the ET microlaser for a pump energy just above the threshold in the direction $\varphi = 0°$ [see Fig. 4(a) for the definition of the azimuthal angle]. The spectrum exhibits a clear structure of equidistant peaks. The Fourier transform of the spectrum, $|{\rm FT}(I)|$, is plotted with respect to the optical length $\ell_{\rm opt}$ in Fig. 3(b). It features several equidistant peaks with diminishing amplitude for increasing $\ell_{\rm opt}$ as expected for a series of equidistant resonances. The first peak at $\ell_{\rm opt} = 843$ μm corresponds to the FSR $\lambda_{\rm FSR} = 0.44$ nm of the lasing spectrum, and the further peaks are harmonics. The two shortest tyes of POs in the ET billiard are Fagano's orbit with $\ell_{\rm geo} = 3a/2 = 450$ μm [see Fig. 4(a)] and the so-called quasi-Fabry-Pérot (qFP) orbits shown in Fig. 4(b). A qFP orbit has two reflections with perpendicular incidence and two reflections with an angle of incidence of 60° with respect to the surface normal. It has a length of $\ell_{\rm geo} = \sqrt{3}a = 519.6$ μm. The whole family of the qFP orbits in the ET can be constructed by shifting one qFP orbit [e.g., the red line in Fig. 4(b)] perpendicularly to its trajectory or rotating it by 120° as indicated by the gray lines. The family of qFP orbits covers the whole surface of the ET. The optical lengths corresponding to Fagano's orbit and the

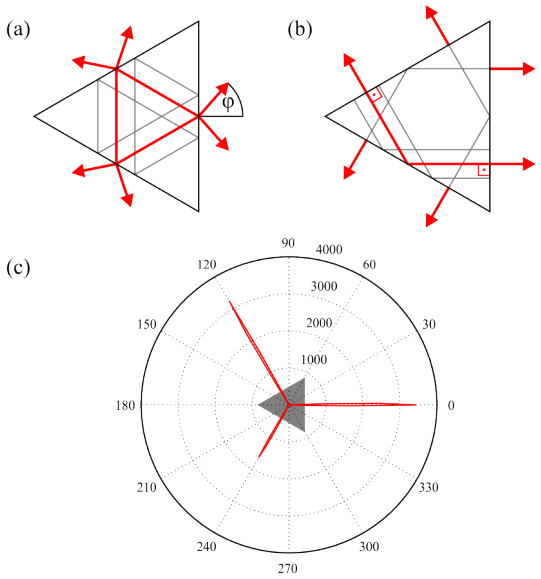

FIG. 4. (a) Examples of the family of Fagano's orbit in the ET billiard. The arrows outside the billiard indicate the corresponding emission directions. The azimuthal angle φ is the angle with respect to the horizontal axis. (b) Examples of the quasi-Fabry-Pérot orbit family (thick red and thin gray lines). The arrows indicate the corresponding emission directions. (c) Measured azimuthal far-field distribution of the ET microlaser. The maximal intensity of the spectrum is plotted with respect to the azimuthal angle φ. The gray triangle in the center indicates the orientation of the cavity.

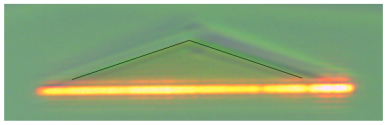

FIG. 5. (Color online) Photo of the lasing ET microlaser in the direction $\varphi = 0°$. The black lines indicate the two other side walls of the cavity.

qFP orbits, respectively, for $n_g = 1.62$ are indicated by the arrows in Fig. 3(b). Obviously, the observed optical length corresponds to the qFP orbit while Fagano's orbit is too short. All the other POs are significantly too long.

Further evidence is gained from the azimuthal emission diagram in Fig. 4(c). The lasing emission is concentrated in the three directions perpendicular to the cavity side walls. This is precisely the behavior expected for modes localized on the qFP orbit as shown in Fig. 4(b). Note that there is no emission from the reflections with angle of incidence 60° since it is larger than the critical angle. On the other hand, Fagano's orbit would correspond to an emission towards, e.g., $\varphi = 48.6°$ as indicated in Fig. 4(a), but no emission is found in these directions. It should be furthermore noted that the lasing threshold of the ET microlaser is only about 17% higher than that of a Fabry-Pérot (FP) cavity of corresponding width. Altogether this demonstrates clearly that the observed lasing modes are localized on the qFP orbit. Finally, a photo taken from the direction $\varphi = 0°$ shows that the whole side wall of the cavity is lasing. This corresponds well to the fact that the family of the qFP orbit covers the whole triangle, though this is also true for all other POs. Photos taken from $\varphi = 120°$ and 240° show the same behavior, whereas no lasing light was observed with the camera in all other directions. In summary, the qFP orbit was identified unambigously from the experimental data as the orbit supporting the lasing modes.

It is at first surprising that the dominant lasing modes are localized on the qFP orbit and not on Fagano's orbit as was the case in Refs. [20, 21]. First, however, the refractive index of the semiconductor materials used in Refs. [20, 21] was significantly higher so that Fagano's orbit was confined by TIR, which is not the case here. Second, the lasing modes that we observed were TE polarized, i.e., their electric field was parallel to the plane of the resonator. In fact, TE polarized modes are favored by the properties of the lasing dye and the pumping scheme that is used here [57]. Since the angle of incidence of Fagano's orbit, 30°, is close to the Brewster angle $\alpha_B = \arctan(1/n) = 33.7°$, a TE mode localized on this PO would suffer from very high losses. From Eq. (3) we calculate $g_{th} = 179.3$ cm^{-1} as the threshold for Fagano's orbit and $g_{th} = 61.9$ cm^{-1} for the qFP orbit. Thus, the dominance of the qFP modes can be well explained by taking into account the peculiarities of the organic microlaser. It should be noted that also the modes of the other triangular microlasers considered in the following were all TE polarized.

Pythagorean triangle (PT)

The next triangle that was investigated is a Pythagorean triangle (PT) with side length ratio 3 : 4 : 5 as shown in Fig. 6. The length of its hypotenuse is 375 μm. It is an example of a irrational right triangle. Both classical and quantum right triangles have been studied and their POs investigated [2, 7, 71]. A property well known by opticians is the fact that a right angle sends a ray back parallel to its initial direction regardless of the angle of incidence. From this follows directly the existence of a family of qFP orbits that impinge perpendicularly on the hypotenuse as shown in Fig. 6. This orbit is a limit case of Fagano's orbit for acute triangles. This and other POs of right triangles can also be constructed by unfolding [2].

The lasing spectrum of the corresponding PT microlaser observed in the direction perpendicular to the hypotenuse is presented in Fig. 7(a). It exhibits a single family of equidistant resonances. Its FT, shown in Fig. 7(b), features a dominant peak at $\ell_{\rm opt} = 1139$ μm.

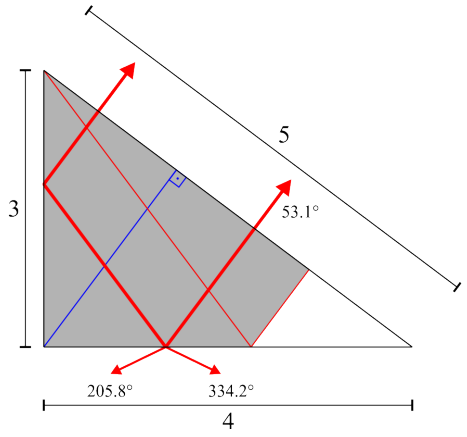

FIG. 6. Pythagorean triangle with side lengths having the ratio 3 : 4 : 5. The thick red line and arrows indicate an example of the qFP orbit family and the corresponding emission directions. The gray area is the surface covered by the qFP orbits that is bounded by the limit orbit indicated as thin red line. The isolated PO along the height of the triangle is indicated as blue line.

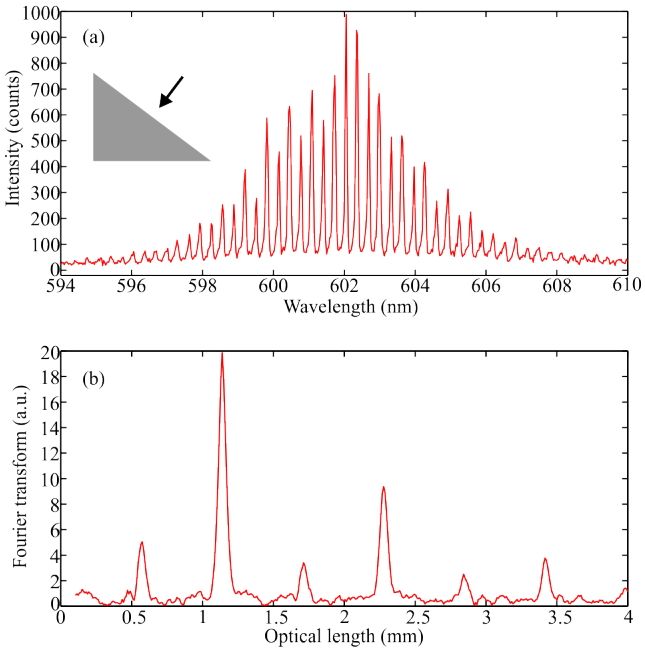

FIG. 7. (a) Spectrum of the PT microlaser. The inset indicates the direction of observation, $\varphi = 53°$. (b) Fourier transform of the spectrum.

This optical length corresponds to the FSR of the spectrum and to the length $\ell_{\rm geo} = 48a/25 = 720$ μm of the qFP orbit. There is a further, smaller peak at half this optical length. It stems from the slight modulation of the resonance amplitudes, i.e., the fact that every other resonance has a somewhat smaller amplitude than its neighbors. It is interesting to note that there is an isolated

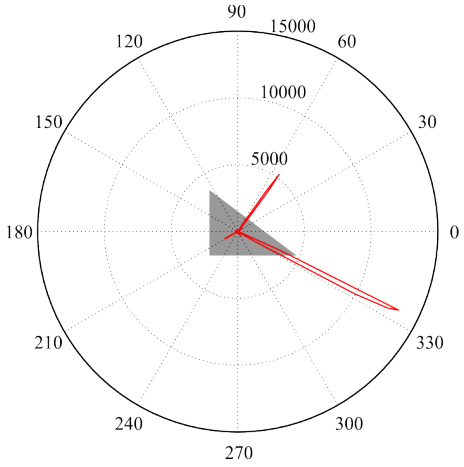

FIG. 8. Far-field distribution of the PT microlaser. The gray triangle in the center indicates the orientation of the cavity.

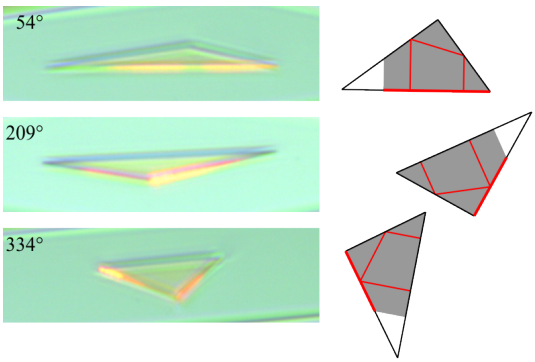

FIG. 9. (Color online) Photos of the PT microlaser (left panels) from the directions 54° (top), 209° (middle), and 334° (bottom). The right panels show the PT triangle with a qFP orbit (thin red line), the area covered by its family (gray), and the parts of the side walls that are hence expected to emit (thick red lines).

PO along the height of the triangle (depicted as blue line in Fig. 6) that has half the length of the qFP orbit. The physical origin of the modulation of the resonance amplitudes and whether it is connected to this PO remains, however, unclear.

The far-field distribution presented in Fig. 8 has three major emission directions, $\varphi = 54°$, 209°, and 334°. These directions correspond well to the ones expected from the qFP orbit according to Snell's law for $n = 1.5$ as indicated in Fig. 6. The lasing spectra in these directions show the same structure as the one in Fig. 7(a). No emission is expected from the left side of the PT since the angle of incidence of the qFP orbit on it is larger than the critical angle. The difference between the amplitudes of the emission lobes at 209° and 334° is an experimental artifact due to imperfections of the alignment of the setup. Photos of the microlaser taken from the three

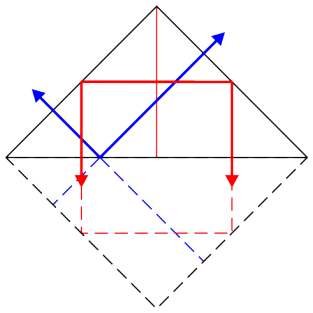

FIG. 10. Right isosceles triangle with the quasi-diamond orbit (thick red line) and the qFP orbit (blue line). The arrows indicate the emission directions of these two POs. The thin red line is the PO along the height of the triangle. The dashed lines indicate the corresponding square billiard and the continuation of the POs in it.

major emission directions are shown in the left panels of Fig. 9. The sketches in the right panels indicate the parts of the side walls that are expected to emit in these directions according to the geometry of the qFP orbits. Indeed, the brightest areas of emission in the photos correspond well to these classical predictions. In contrast, also some weak emission is observed from the side wall on the left hand side at 209° and from the side wall at the right hand side at 334° which is not predicted. In summary, the spectra, the far-field distribution and the photos clearly evidence that the observed lasing modes are localized on the qFP orbits, even though not all details can be explained by ray dynamics.

Right isosceles triangle (RIT)

The second right triangle that was investigated is the right isosceles triangle (RIT) which is a essentially a square cut in half along the diagonal. The right isosceles triangle billiard is, like the square billiard, integrable. The two shortest and simplest POs of the RIT are the qFP orbit and the quasi-diamond (qD) orbit which is named after the corresponding PO in the square billiard as demonstrated in Fig. 10. Both PO families cover the whole area of the billiard. Two spectra measured perpendicularly to the hypotenuse and one of the short sides, respectively, are shown in Fig. 11. Both spectra consist of families of equidistant resonances that have, however, a different FSR each. The largest peak in the FT of the spectrum for $\varphi = 270°$ is at $\ell_{\rm opt} = 1270$ μm. This corresponds to the qD orbit with length $\ell_{\rm geo} = 2a = 789.6$ μm as expected for this direction, where the length of the hypotenuse is $a = 394.8$ μm. The FT also features a smaller peak at half this optical length. In complete analogy to the case of the PT, this small peak stems from a modulation of the resonance amplitudes, and there is a PO along the height of the triangle with

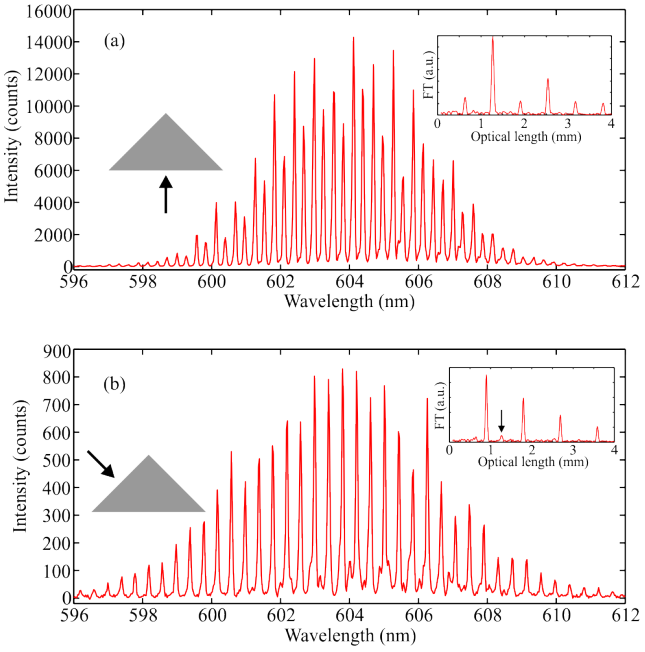

FIG. 11. (a) Spectrum of the RIT microlaser measured in the direction $\varphi = 270°$ (see left inset). The right inset shows the FT of the spectrum. (b) Spectrum of the RIT microlaser measured in the direction $\varphi = 135°$ (see left inset). The right inset shows the FT of the spectrum, with the arrow indicating a small peak at $\ell_{\rm opt} = 1270$ μm.

half the length of qD orbit [see Fig. 10]. In contrast, the FT of the spectrum at $\varphi = 135°$ shows a peak at $\ell_{\rm opt} = 894$ μm. This corresponds to the qFP orbit with length $\ell_{\rm geo} = \sqrt{2}a = 558.3$ μm. An unexpected finding is a small peak at $\ell_{\rm opt} = 1270$ μm [indicated by the black arrow in the inset of Fig. 11(b)] that corresponds to the qD orbit. It originates from another family of barely visible resonances in the spectrum.

The far-field distribution shown in Fig. 12 features several emission lobes with differing amplitudes. The strongest emission lobe is in the direction of $\varphi = 270°$ and is due to the qD orbit as discussed above. It was cropped in Fig. 12 since its amplitude of $\approx 26,000$ counts far exceeds that of the other emission lobes. The asymmetry between the emission lobes to the left and to the right is an experimental artifact as in the case of the PT. The lobes at 45° and 135° correspond to the qFP orbit. All this is in perfect agreement with the classical predictions shown in Fig. 10. However, there are also small contributions of the qD orbit in the directions of 45° and 135° as discussed above, and two additional small lobes at $\varphi = 225°$ and 315° that are also related to the qD orbit.

The origin of these can be elucidated by the photos shown in Fig. 13. The photos taken from $\varphi = 45°$ show a strong emission from the sidewall perpendicular to the camera as predicted for the qFP orbit. Classically, it

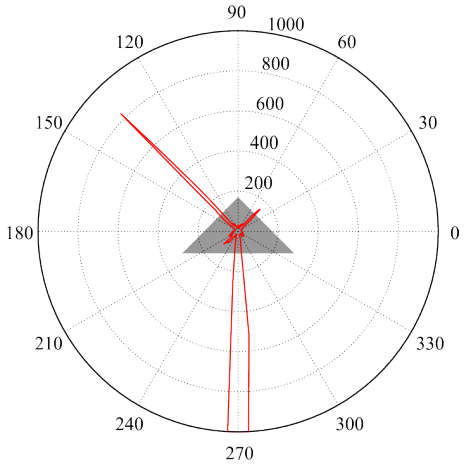

FIG. 12. Far-field distribution of the RIT microlaser. The gray triangle in the center indicates the orientation of the cavity.

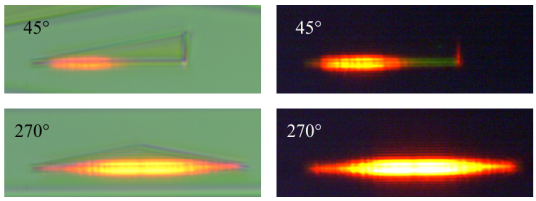

FIG. 13. (Color online) Photos of the RIT microlaser taken from 45° (top row) and 270° (bottom row) with background illumination (left panels) and without (right panels).

is expected that the whole side wall emits like in Fig. 5 since the qFP orbit family covers the whole RIT. Why this is not observed experimentally remains unclear. In addition, there is a weak emission from the sidewall parallel to the camera perspective, best seen without background illumination. A similar grazing emission was also observed at $\varphi = 135°$, 225°, and 315°. It is not expected classically since the qD orbit is totally reflected at the two short sides. The same kind of grazing emission is also observed for the diamond orbit modes of square organic microlasers and will be discussed elsewhere [72]. The photo taken at $\varphi = 270°$ finally shows emission from the whole hypotenuse as expected for modes localized on the qD orbit.

The key characteristics of the RIT microlaser can be explained well by simple POs of the corresponding billiard as in the cases of the ET and PT. But the RIT microlaser is an even more interesting case than the previously treated triangles because it features two families of modes localized on different POs that coexist. A calculation of the thresholds according to Eq. (3) reveals that they are very close to each other since both POs have nearly the same length and losses. This prediction agrees qualitatively with the measured thresholds.

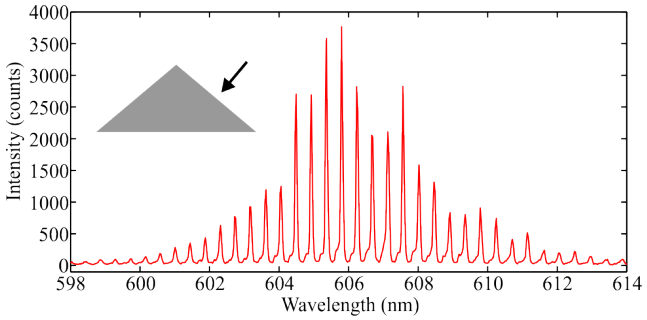

FIG. 14. Spectrum of the isosceles 100° microlaser. The inset shows the geometry of the laser and the angle of observation.

Another point of interest is the grazing emission of the modes localized on the qD orbit that is not expected from the ray dynamics. It demonstrates that some properties of the microlaser call for a more careful treatment taking into account wave-dynamical effects.

Isosceles triangle with top angle 100° (IT100)

The simplest class of triangles with a symmetry are isosceles triangles. Microlasers with isosceles triangle shape have been investigated for example in Ref. [34]. The POs of isosceles triangles can be constructed via the unfolding technique analogously to right triangles [2]. The simplest PO that exists in all isosceles triangles is the qFP orbit already known from the RIT. Another, more complicated example is the double-bowtie (DB) orbit shown in Fig. 2. It exists for top angles between 90° and 111.5°. The first of two obtuse isosceles triangles that are discussed here is the one with top angle $\alpha = 100°$ (abbreviated IT100 in the following). Its classical dynamics is pseudo-integrable with genus $g = 4$.

The spectrum of the IT100 microlaser measured in the direction $\varphi = 50°$, i.e., perpendicular to one of the short side walls, is shown in Fig. 14. The FSR of the equidistant resonance family corresponds to an optical length of $\ell_{\rm opt} = 833$ μm. The underlying PO is hence the qFP orbit shown in Fig. 15(a) that has a length $\ell_{\rm geo} = 2a\sin(40°) = 514.2$ μm, where the length of the hypotenuse is $a = 400$ μm. The far-field distribution presented in Fig. 15(b) shows four major emission lobes. Their directions, $\varphi = 50°$, 130°, 194°, and 344°, are precisely the ones expected classically for the qFP orbit. There are also some smaller emission lobes at, e.g., 240° and 300°, hardly visible in Fig. 15(b). The spectra in these directions also have a FSR corresponding to the qFP orbit. These directions cannot, however, be explained by the ray dynamics. Hence, the major features of the IT100 microlaser are in very good agreement with the classical predictions, while some details are beyond a simple ray-dynamical analysis, as in the previous cases.

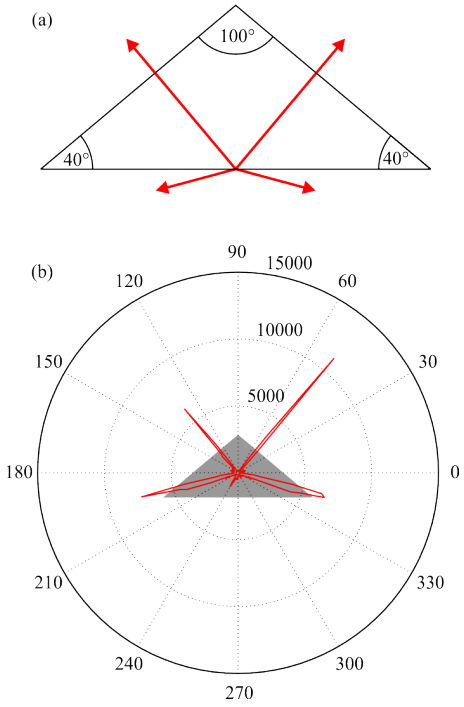

FIG. 15. (a) Geometry of the isosceles 100° triangle. A qFP orbit and its emission directions are indicated as red line and red arrows, respectively. (b) Far-field distribution of the IT100 microlaser. The gray triangle in the center indicates the orientation of the cavity.

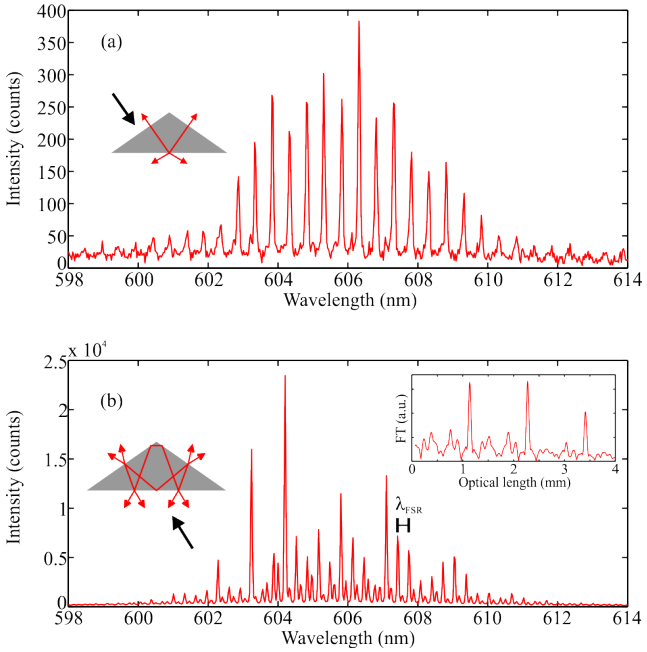

FIG. 16. (a) Spectrum of the IT110 microlaser measured at $\varphi = 125°$. The inset indicates the geometry of the triangle, a qFP orbit (red lines) and its emission directions (red arrows) as well as the observation direction (black arrow). (b) Spectrum of the IT110 microlaser measured at $\varphi = 302°$. The inset indicates the geometry of the triangle, the DB orbit (red lines) and its emission directions (red arrows) as well as the observation direction (black arrow).

Isosceles triangle with top angle 110° (IT110)

The second isosceles triangle that was investigated is the one with top angle 110° (abbreviated IT110 in the following). It is also pseudo-integrable, with genus $g = 17$. The spectrum of the IT110 microlaser at $\varphi = 125°$ is shown in Fig. 16(a). It shows a single family of resonances, the FSR of which corresponds to $\ell_{\rm opt} = 744$ μm. The corresponding PO is again the qFP orbit with length $\ell_{\rm geo} = 2a\sin(35°) = 458.9$ μm, where the length of the hypotenuse is $a = 400$ μm. Another spectrum measured at $\varphi = 302°$ is presented in Fig. 16(b). Its structure is less clear than that of the one at 125°, but its FT (shown as inset) shows a clear peak at $\ell_{\rm opt} = 1139$ μm and multiples of this length. The corresponding FSR of $\lambda_{\rm FSR} = 0.32$ nm is indicated in the spectrum. It is the FSR of the dominant family of modes, with additional smaller resonances in between. This optical length as well as the azimuthal direction correspond well to the DB orbit (shown again as inset) with a length of $\ell_{\rm geo} = a[1 - \cos(140°)] = 706.4$ μm. It should be noted that the threshold of the modes localized on the qFP orbit is almost three times higher than that of the modes localized on the DB orbit, which agrees qualitatively with the prediction by Eq. (3).

The far-field distribution of the IT110 microlaser is presented in Fig. 17. The six principal emission directions are indicated by the black arrows and match very well the predictions for the DB orbit [see inset of Fig. 16(b)]. The amplitudes of the emission lobes lack, however, the expected symmetry as in previous cases. No emissions lobes corresponding to the qFP orbit were observed since the microlaser was pumped slightly above the threshold of the DB orbit modes, but well below the threshold of the qFP orbit modes. The photos shown in Fig. 18 were taken with the same pump intensity as for the measurement of the far-field distribution. The directions of observation correspond to the major emission directions. All photos show that the most intense part of the laser emission originates from those parts of the side walls that are covered by the family of the DB orbit (indicated by the red lines in the drawing of the IT110). This confirms that the lasing modes with the lowest threshold are indeed localized on the DB orbit. However, the photos also show weak emission from other parts of the side walls that are not covered by the family of the DB orbit, similar to the case of the PT microlaser. A possible explanation is that even though the field distributions of superscarred resonant states are strongly concentrated inside the PO channel, they also have a nonvanishing field outside of the PO channel due to coupling to nonscarred

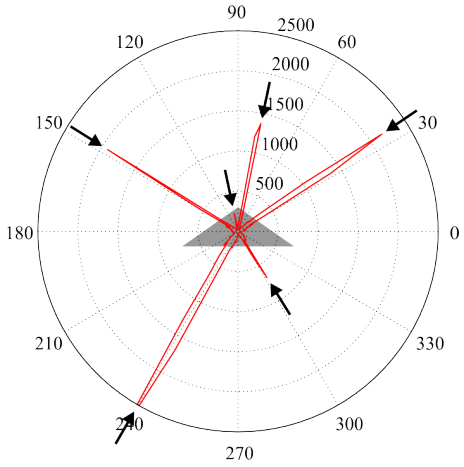

FIG. 17. Far-field distribution of the IT110 microlaser. The six major emission directions are indicated by the black arrows. The lobe at 240° was cropped due to the magnified scale of the figure. The gray triangle in the center indicates the orientation of the cavity.

states [46, 73, 74].

In conclusion, the IT110 microlaser is another example like the RIT where two families of modes localized on different POs coexist. In contrast to the case of the RIT, however, there is a significant difference between the thresholds of the two mode families so that one of them is easily selected by keeping the pump intensity sufficiently low. It should furthermore be noted that the dominant PO, the DB orbit, is selected because it has the lowest losses even though it is longer and more complicated than the qFP orbit. Thus, the change of a single geometrical parameter (the top angle in this case) allows to significantly alter the lasing characteristics. A more detailed study of the parametric dependence of the lasing characteristics of isosceles triangles would hence be interesting.

Quasi-equilateral triangle (QET)

While all the triangles considered so far had symmetries or other properties that enabled an easy construction of their POs, the case considered in the following has none of these. It is a deformation of the equilateral triangle and hence called quasi-equilateral triangle (QET) in the following. Its side lengths are $a = 316.7$ μm, $0.95a = 308.8$ μm, and $0.9a = 285.0$ μm, respectively, as indicated in Fig. 19. It is an irrational triangle and we hence cannot easily construct any POs besides Fagano's orbit. In particular, the qFP orbits no longer exist due to the lack of symmetry.

A typical spectrum, observed at $\varphi = 267°$, is shown in Fig. 20(a). The structure of the spectrum is not as clear as for the previously shown ones, nonetheless some small sequences of equidistant resonances can be identified. The FT of the spectrum shows a peak at $\ell_{\text{opt}} = 830$ μm and its approximate multiples. The corresponding FSR of 0.44 nm indeed matches that of the resonances in the spectrum. This optical length is close to that of the qFP orbit in an ET of the same base side length, however, the qFP orbit no longer exists due to the deformation. There are, however, three diffractive POs along the heights of the triangle that have nearly the same lengths. They are indicated by the colored lines in Fig. 19 and called A, B, and C in the following. They are called diffractive because one of their vertices is at a diffractive corner of the billiard (see Sec.). Their lengths are $\ell^A_{\text{geo}} = 518.2$ μm, $\ell^B_{\text{geo}} = 547.0$ μm, and $\ell^C_{\text{geo}} = 492.2$ μm, respectively. The respective optical lengths are indicated by arrows in Fig. 20(b) where the group refractive index $n_g = 1.60$ was determined from measurements of Fabry-Pérot cavities on the same sample. Their optical lengths are indeed close to the peaks observed in the FT of the spectrum.

The far-field distribution of the QET microlaser is plotted in Fig. 21(a). It features three broad bundles of emission lobes that are roughly perpendicular to the cavity side walls. The FT of the spectra measured at different azimuthal angles is shown in Fig. 21(b). The dominant optical lengths vary somewhat with φ, but they always stay close to the lengths of the three diffractive POs the optical lengths of which are indicated by the vertical white lines. This corresponds to the fact that the spectra always feature a similar FSR even though their stucture and quality varies significantly, leading to a relatively high noise level in the FT. No evidence of Fagano's orbit was found like in the case of the ET. So while the FSRs approximately match those corresponding to the diffractive orbits, other observations do not fit to modes localized on them. For example, the directions of maximal emission are not exactly perpendicular to the side walls as one would naively expect.

The photos shown in Fig. 22 enable a better understanding of the nature of the resonant modes. They show the lasing QET from the directions approximately perpendicular to the side walls. All of them show that the points of origin of the lasing emission are more or less broadly distributed over the side walls. The expectation from modes localized on the diffractive POs, in contrast, would be that the origin of emission is strongly concentrated around the feet of the heights that are roughly in the middle of the side walls. Another expectation for this kind of mode would be strong emission coming from the corners of the triangle. This is, however, not observed in any direction. In fact, the images shown in Fig. 22 are typical also for other directions in which the QET microlaser emits.

In conclusion, the lasing characteristics of the QET microlaser cannot be well explained by localization on diffractive or nondiffractive POs of the QET billiard. The observed FSRs correspond to a length similar to that of

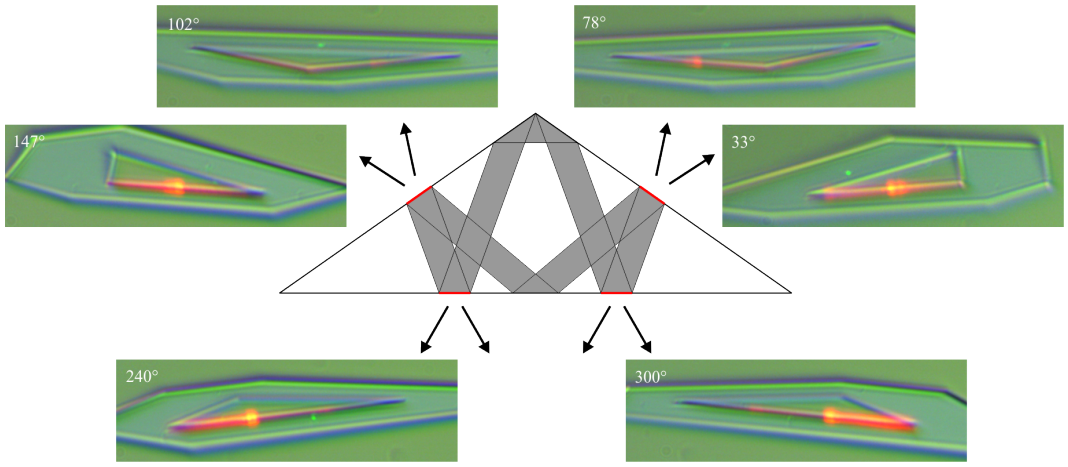

FIG. 18. (Color online) Photos of the IT110 microlaser taken from the main emission directions of the modes localized on the DB orbit. The sketch in the center indicates the area in the IT110 that is covered by the family of the DB orbit (gray) and the parts of the side walls that are hence predicted to emit (red).

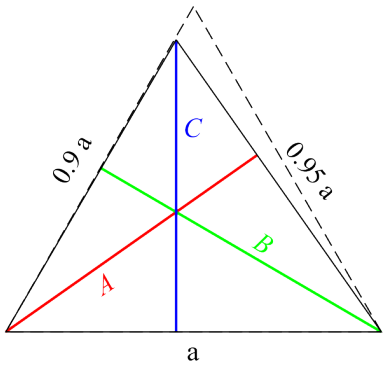

FIG. 19. Geometry of the quasi-equilateral triangle. The side length in units of the base side length a are indicated. The red, green, and blue lines along the heights of the triangle indicate the diffractive POs A, B, and C, respectively. The dashed lines indicate an equilateral triangle with the same base length for comparison.

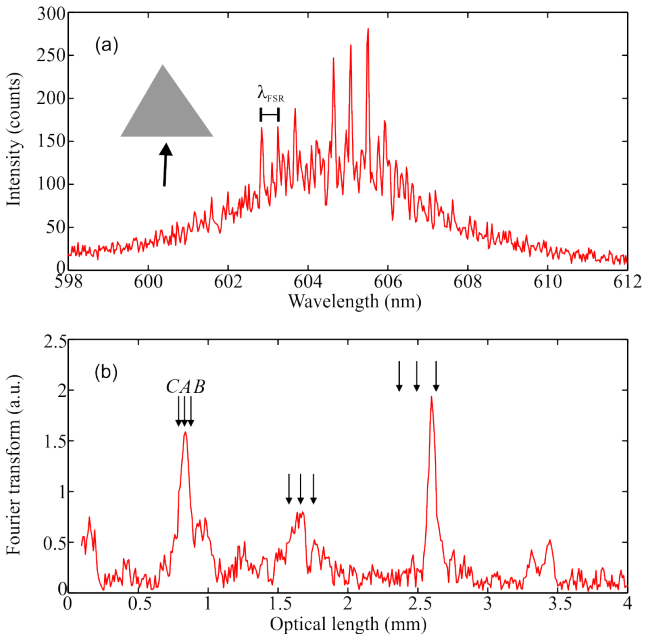

FIG. 20. (a) Spectrum of the QET microlaser. The observation angle of $\varphi = 267°$ is indicated in the inset. The indicated FSR corresponds to the dominant peak in the FT of the spectrum. (b) FT of the spectrum. The triplets of arrows indicate the optical lengths of the three diffractive POs A, B, and C and their multiples, respectively.

the qFP orbits of an ET. A possible explanation is that the observed modes are the perturbed modes of the ET microlaser that were localized on the qFP orbit. Due to the small perturbation, their FSR stays approximately the same, but the far-field distribution broadens around the emission directions perpendicular to the side walls of the qFP orbit. The same effect was observed in Ref. [60] for triangular resonators with Dirichlet boundary conditions. Some modes were shown to be localized on so-called ghost POs, i.e., the POs of a geometrically different, but similar triangle. An analogous case is the persistence of the influence of the bouncing ball orbits in a quantum stadium billiard when the originally parallel side walls of the stadium are slightly tilted [61]. The reason for these effects is that while the classical dynamics can exhibit singular behavior with respect to perturbations of the billiard geometry, e.g., POs suddenly vanishing completely, wave-dynamical systems react in a continuous manner to geometrical perturbations, essentially smoothing out the singularities of classical mechanics. The data presented here leads us to believe that the modes of the QET microlasers are indeed localized on

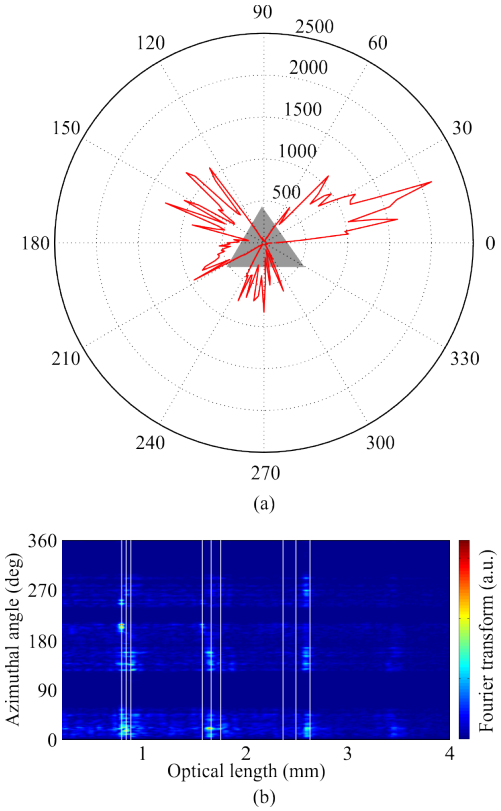

FIG. 21. (a) Far-field distribution of the QET microlaser. The gray triangle in the center indicates the orientation of the cavity. (b) FT of the spectra with respect to the optical length and azimuthal angle φ. The vertical white lines indicate the optical lengths of the three diffractive POs and their multiples.

the ghost qFP orbit, but numerical investigations of the wave functions will be necessary to confirm this.

Quasi-isosceles triangle (QIT)

The next case is a deformation of one of the previous triangles like the QET. The triangle was consructed by moving the right vertex of the IT100 by 10 μm to the left while keeping the other two vertices fixed as demonstrated in Fig. 23(a). Hence we call it quasi-isosceles triangle (QIT). It is irrational and hence no simple POs are known *a priori* since the qFP and the DB orbit of the IT100 are destroyed by the geometric perturbation. There are, however, three diffractive POs similar to the case of the QET as shown in Fig. 23(b). One is along the height of the triangle (called HPO in the following), and the other two have one perpendicular reflection at a short sidewall and one at the top vertex. They can be considered as the remnants of the qFP orbits of the IT100 and are hence called diffractive quasi-Fabry-Pérot (dqFP) orbits in the following.

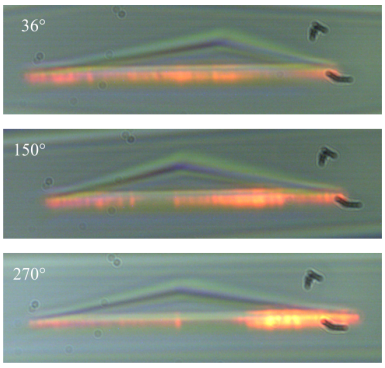

FIG. 22. (Color online) Photos of the QET microlaser taken from the directions perpendicular to the side walls, 36° (top), 150° (middle), and 270° (bottom).

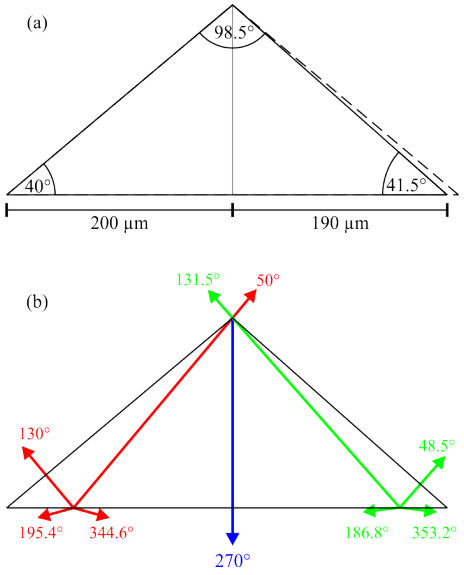

FIG. 23. (a) Geometry of the quasi-isosceles triangle. It is a deformation of the isosceles triangle with top angle 100° that is indicated by the dashed lines. (b) Three simple diffractive POs of the QIT. The red and green lines indicate the two dqFP orbits, respectively, and the blue line the HPO. The arrows indicate the corresponding emission directions.

Two spectra of the QIT microlaser observed in different directions are plotted in Fig. 24. Both spectra show a relatively clear structure of equidistant modes. Their FSRs, however, differ, and hence the corresponding optical length as can be seen in the FTs shown as insets. The optical length in the case of the spectrum for $\varphi = 62°$ is $\ell_{\rm opt} = 546$ μm. This can only correspond to the length of the HPO, $\ell_{\rm geo} = 335.6$ μm. The optical length for the spectrum for $\varphi = 332°$ is 819 μm and corresponds approximately to the lengths of the two dqFP orbits. The length of the left dqFP orbit [red line in Fig. 23(b)] is $\ell_{\rm geo} = 514.2$ μm and is identical to the length of the qFP

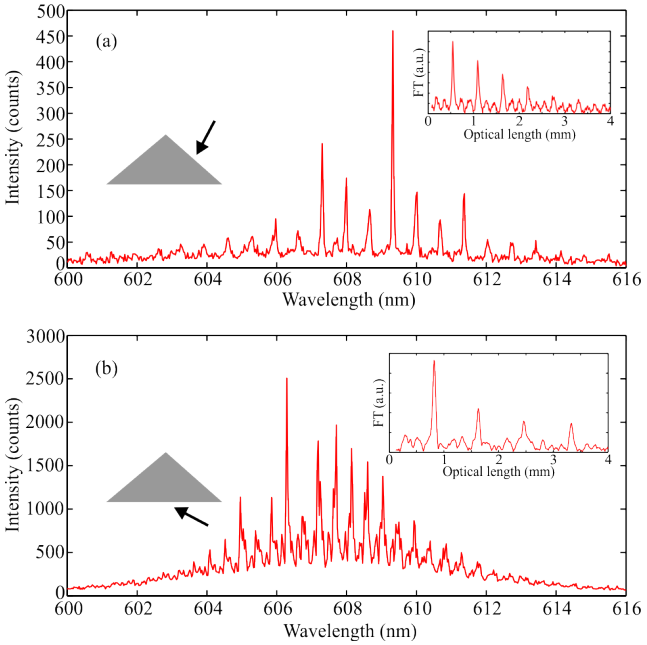

FIG. 24. (a) Spectrum of the the QIT microlaser observed at $\varphi = 62°$. The insets indicate the orientation of the triangle and the FT of the spectrum, respectively. (b) Spectrum of the the QIT microlaser observed at $\varphi = 332°$. The insets indicate the orientation of the triangle and the FT of the spectrum, respectively.

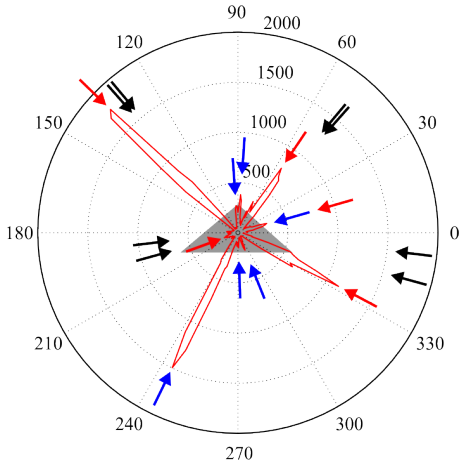

FIG. 25. Far-field distribution of the QIT microlaser. The gray triangle in the center indicates the orientation of the cavity. The red and blue arrows indicate the directions in which the FT of the spectrum exhibited the optical length of the dqFP and / or the height orbit, respectively. The black arrows indicate the emission directions predicted for the dqFP orbits in Fig. 23(b).

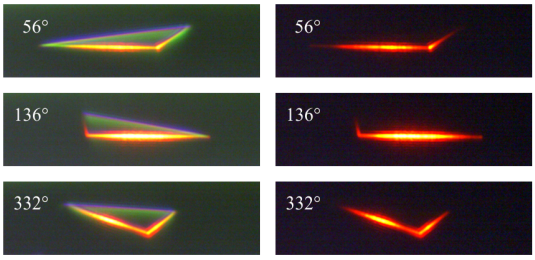

FIG. 26. (Color online) Photos of the QIT microlaser taken in the main emission directions featuring the optical length of the dqFP orbits, 56° (top), 136° (middle), and 332° (bottom), with background illumination (left panels) and without (right panels).

orbit in the IT100, while the length of the right dqFP orbit [green line in Fig. 23(b)] is $\ell_{\text{geo}} = 503.1\ \mu$m. So the QIT microlaser exhibits (at least) two different families of modes that have similar thresholds. Next, we investigated which family of modes emits in which directions. This is depicted in Fig. 25. The far-field distribution shows a large number of emission lobes with varying amplitudes, though the emission is not as broadly distributed as in the case of the QET. The directions in which the spectra exhibit the optical length of the qdFP orbits and the HPO are indicated by the red and blue arrows, respectively. Note that for some of the smaller emission lobes the corresponding optical length could not be clearly determined due to indistinct spectra. In fact, the most prominent emission lobes point approximately in the directions expected for a dqFP or height orbit, respectively. There remain, however, significant deviations between the emission directions of the presumed dqFP modes and the directions predicted by ray optics that are indicated by the black arrows. These deviations cannot be consistently explained by a different refractive index either. Regarding the presumed HPO modes, there are several emission lobes around, though not precisely in, the direction of 270° predicted classically. Furthermore, the two emission lobes close to 90° seem reasonable for such modes, too. The strong emission in the direction of $\varphi = 244°$ from the presumed HPO modes and in the direction of 16° from both families of modes, however, defy any simple ray-dynamical explanation.

The photos taken in the main emission directions of the presumed dqFP modes are presented in Fig. 26. They show that the emission originates from almost the whole side walls and not just small portions of it as would be expected for the isolated dqFP orbits. The photos rather resemble those of the ET and RIT microlasers. In addition, a part of the emission originates from those side walls that are not directly facing the camera. Emission from these side walls is not at all expected from any Fabry-Pérot-like modes. The photos in Fig. 27 were analogously taken at the main emission directions of the presumed HPO modes. The lasing emission is not as broadly distributed along the side walls as in the previous cases in Fig. 26, but shows nonetheless no single points

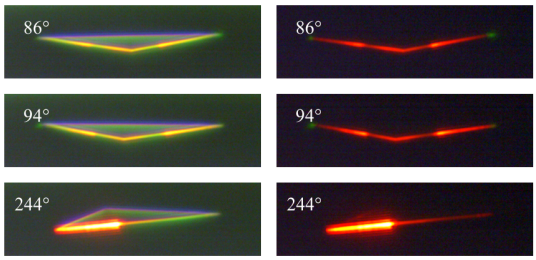

FIG. 27. (Color online) Photos of the QIT microlaser taken in the main emission directions featuring the optical length of the HPO, 86° (top), 94° (middle), and 244° (bottom), with background illumination (left panels) and without (right panels).

of concentration. In particular, the photos at $\varphi = 86°$ and 94° demonstrate that the emission in these directions is not predominantly originating from the vertex of the triangle as expected for a mode localized on the diffractive height orbit. In summary, the photos evidence that both families of lasing modes cover more or less the whole microlaser and are not strongly concentrated along the isolated diffractive orbits shown in Fig. 23. We are hence led to believe that the one family of modes is localized on the ghost qFP orbits, i.e., they are the perturbed qFP modes of the IT100, analogously to the case of the QET. The situation for the other family of modes with an FSR corresponding to the HPO is less clear since a (nondiffractive) height PO does not exist in the IT100, and no family of modes with a similar FSR was observed for the IT100 microlaser. In any case further investigations are necessary for a full understanding, in particular of those features that do not in any way correspond to classical trajectories. It is interesting to note that even though a PO is known to exist in the QIT since its angles are all less than 100°, the dominant lasing modes are clearly not localized on any (classical) PO. It can be presumed that even the shortest PO in the QIT is too long or has to high losses to support lasing modes with a reasonbly low threshold, and that therefore other types of lasing modes are predominant.

CONCLUSIONS

While there are still open questions regarding the properties and existence of POs in classical triangular billiards and this remains a field of active research, it is also highly interesting to explore the influence of the POs on the properties of the corresponding wave-dynamical billiards. Of particular interest are billiards the POs of which are not known or at least not evident since of complicated shape. One of the objectives of the experiments presented here was therefore to see whether the resonant states in these cases are localized on classical POs, and if yes, on which ones, or if they have no more relation to ray optics. We investigated this ray-wave correspondence in experiments with organic microlasers of triangular shape. The sizes of the microlasers were chosen very large compared to the wavelength in order to ensure the validity of ray-based models and to provide sufficient gain. The shapes that were chosen correspond to different types of classical dynamics featuring different POs and were hence expected to give rise to diverse lasing characteristics.

Several examples of triangles with well-understood classical dynamics and relatively simple POs were studied. They all exhibited lasing modes that were clearly localized on various POs, and their major features like the dominant emission directions could be predicted by ray optics. It seems to be a general rule for polygonal billiards having simple, short POs with not too high losses that the modes of the corresponding microlasers are localized on these POs [19, 22, 49, 52]. However, some details of the observed spectra and far-field distributions are clearly beyond simple ray-dynamical explanations, and hence also wave-dynamical effects need to be taken into account. This underlines the need to further develop and refine the different models of modal localization in dielectric resonators.

Furthermore, two examples of triangles lacking symmetry and hence any simple POs were investigated. Both cases were deformations of previously investigated triangles. Their modes seemed to be localized on ghost POs [60], i.e., they resembled the modes localized on POs of the undeformed triangles. But even though their modes retained some of the features of those of the unperturbed triangles, their properties like the major emission directions could at best be explained on a qualitative level. These examples demonstrate that the simple ray-based models used for other triangles fail if there are no longer any simple POs. It hence remains an interesting challenge to better understand these cases by further experimental and numerical studies or by means of perturbation theory [75, 76].

It should be noted that we relied almost exclusively on the passive cavity states in order to understand the lasing properties. This is reasonable since it sufficed to explain the principal features of the microlasers and the pump intensity remained close to the lasing threshold in most cases. Investigating the lasing behavior well above threshold would be an interesting future project and might reveal different types of modes than those reported here. Of particular interest is, however, a better understanding of the thresholds and of the mode competition since several microlasers exhibited two or more coexisting families of modes. The simple PO-based estimate for the threshold used here proved to be correct on a qualitative level, however, more refined methods are necessary for a quantitative prediction of the lasing thresholds and to understand the lasing behavior in the presence of competing mode types.

The authors are grateful to E. Bogomolny for illuminating discussions. S. B. gratefully acknowledges funding from the PALM LABEX and the European Union Seventh Framework Programme (FP7/2007-2013) under Grant Agreement No. 246.556.10.

[1] W. A. Veech, Inventiones mathematicae **97**, 553 (1989).
[2] B. Cipra, R. M. Hanson, and A. Kolan, Phys. Rev. E **52**, 2066 (1995).
[3] E. Gutkin, The American Mathematical Monthly **104**, 618 (1997).
[4] M. Boshernitzan, G. Galperin, T. Krüger, and S. Troubetzkoy, Trans. Am. Math. Soc. **350**, 3523 (1998).
[5] R. Kenyon and J. Smillie, Commentarii Mathematici Helvetici **75**, 65 (2000).
[6] R. E. Schwartz, Experimental Mathematics **15**, 161 (2006).
[7] W. P. Hooper, Geometriae Dedicata **125**, 39 (2007).
[8] M. C. Gutzwiller, *Chaos in Classical and Quantum Mechanics*, Interdisciplinary Applied Mathematics, Vol. 1 (Springer, New York, 1990).
[9] H.-J. Stöckmann, *Quantum Chaos: An Introduction* (Cambridge University Press, Cambridge, UK, 2000).
[10] S. Sridhar, Phys. Rev. Lett. **67**, 785 (1991).
[11] H.-J. Stöckmann and J. Stein, Phys. Rev. Lett. **64**, 2215 (1990).
[12] A. Richter, in *Emerging Applications of Number Theory*, The IMA Volumes in Mathematics and its Applications, Vol. 109, edited by D. A. Hejhal, J. Friedman, M. C. Gutzwiller, and A. M. Odlyzko (Springer, New York, 1999) pp. 479–523.
[13] P. Bertelsen, C. Ellegaard, T. Guhr, M. Oxborrow, and K. Schaadt, Phys. Rev. Lett. **83**, 2171 (1999).
[14] H. G. L. Schwefel, H. E. Tureci, A. D. Stone, and R. K. Chang, "Progress in asymmetric resonant cavities: Using shape as a design parameter in dielectric microcavity lasers," Optical Processes in Microcavities, World Scientific (2003).
[15] A. B. Matsko, ed., *Practical Applications of Microresonators in Optics and Photonics* (CRC Press, Boca Raton, 2009).
[16] H. E. Tureci, H. G. L. Schwefel, A. D. Stone, and E. E. Narimanov, Opt. Express **10**, 752 (2002).
[17] C. Gmachl, E. E. Narimanov, F. Capasso, J. N. Baillargeon, and A. Y. Cho, Opt. Lett. **27**, 824 (2002).
[18] T. Harayama, T. Fukushima, P. Davis, P. O. Vaccaro, T. Miyasaka, T. Nishimura, and T. Aida, Phys. Rev. E **67**, 015207 (2003).
[19] M. Lebental, N. Djellali, C. Arnaud, J.-S. Lauret, J. Zyss, R. Dubertrand, C. Schmit, and E. Bogomolny, Phys. Rev. A **76**, 023830 (2007).
[20] H. C. Chang, G. Kioseoglou, E. H. Lee, J. Haetty, M. H. Na, Y. Xuan, H. Luo, A. Petrou, and A. N. Cartwright, Phys. Rev. A **62**, 013816 (2000).
[21] J. Yoon, S.-J. An, K. Kim, J. K. Ku, and O. Kwon, Appl. Opt. **46**, 2969 (2007).
[22] E. Bogomolny, N. Djellali, R. Dubertrand, I. Gozhyk, M. Lebental, C. Schmit, C. Ulysse, and J. Zyss, Phys. Rev. E **83**, 036208 (2011).
[23] I. Braun, G. Ihlein, F. Laeri, J. U. Nöckel, G. Schulz-Ekloff, F. Schüth, U. Vietze, Ö. Weiß, and D. Wöhrle, Appl. Phys. B **70**, 335 (2000).
[24] H.-T. Lee and A. W. Poon, Opt. Lett. **29**, 5 (2004).
[25] C. Li, L. Zhou, S. Zheng, and A. W. Poon, IEEE J. Sel. Top. Quant. Electronics **12**, 1438 (2006).
[26] E. Marchena, S. Shi, and D. Prather, Opt. Express **16**, 16516 (2008).
[27] C. C. Chen, K. W. Su, Y. F. Chen, and K. F. Huang, Opt. Lett. **33**, 509 (2008).
[28] R. C. C. Chen, Y. T. Yu, Y. J. Huang, C. C. Chen, Y. F. Chen, and K. F. Huang, Opt. Lett. **34**, 1810 (2009).
[29] Y.-F. Chen, Y.-T. Yu, Y.-J. Huang, P.-Y. Chiang, K.-W. Su, and K.-F. Huang, Opt. Lett. **35**, 2723 (2010).
[30] Y. F. Chen, Y. T. Yu, P. Y. Chiang, P. H. Tuan, Y. J. Huang, H. C. Liang, and K. F. Huang, Phys. Rev. E **83**, 016208 (2011).
[31] T. Nobis and M. Grundmann, Phys. Rev. A **72**, 063806 (2005).
[32] D. Yu, Y. Chen, B. Lia, X. Chen, M. Zhang, F. Zhao, and S. Ren, Appl. Phys. Lett. **91**, 091116 (2007).
[33] J. Dai, C. X. Xu, K. Zheng, C. G. Lv, and Y. P. Cui, Appl. Phys. Lett. **95**, 241110 (2009).
[34] M. S. Kurdoglyan, S.-Y. Lee, S. Rim, and C.-M. Kim, Opt. Lett. **29**, 2758 (2004).
[35] G. Fonte and B. Zerbo, Eur. Phys. J. Plus **127**, 8 (2012).
[36] P. J. Richens and M. V. Berry, Physica D **2**, 495 (1981).
[37] S. Kerckhoff, H. Masur, and J. Smillie, Annals of Mathematics **124**, 293 (1986).
[38] A. Katok and B. Hasselblatt, *Introduction to the Modern Theory of Dynamical Systems* (Cambridge University Press, Cambridge, 1995).
[39] W. P. Hooper, Proc. Am. Math. Soc. **141**, 857 (2013).
[40] R. W. Robinett, J. Math. Phys. **40**, 101 (1999).
[41] M. Brack and R. K. Bhaduri, *Semiclassical Physics* (Westview Press, Oxford, 2003).
[42] M. C. Gutzwiller, J. Math. Phys. **11**, 1791 (1970).
[43] M. C. Gutzwiller, J. Math. Phys. **12**, 343 (1971).
[44] E. J. Heller, Phys. Rev. Lett. **53**, 1515 (1984).
[45] E. Bogomolny and C. Schmit, arXiv:nlin/0402017v1 **0**, 0 (2004).
[46] E. Bogomolny, B. Dietz, T. Friedrich, M. Miski-Oglu, A. Richter, F. Schäfer, and C. Schmit, Phys. Rev. Lett. **97**, 254102 (2006).
[47] E. Bogomolny, R. Dubertrand, and C. Schmit, Phys. Rev. E **78**, 056202 (2008).
[48] E. Bogomolny and R. Dubertrand, Phys. Rev. E **86**, 026202 (2012).
[49] S. Bittner, E. Bogomolny, B. Dietz, M. Miski-Oglu, P. Oria Iriarte, A. Richter, and F. Schäfer, Phys. Rev. E **81**, 066215 (2010).
[50] S. Shinohara, T. Harayama, and T. Fukushima, Opt. Lett. **36**, 1023 (2011).
[51] Q. Song, L. Ge, J. Wiersig, and H. Cao, Phys. Rev. A **88**, 023834 (2013).
[52] S. Bittner, E. Bogomolny, B. Dietz, M. Miski-Oglu, and A. Richter, Phys. Rev. E **88**, 062906 (2013).
[53] E. Bogomolny and C. Schmit, Nonlinearity **16**, 2035 (2003).
[54] G. Gennarelli and G. Riccio, IEEE Trans. Antennas Propag. **59**, 898 (2011).
[55] E. Bogomolny, Physica D **31**, 169 (1988).
[56] N. Bachelard, J. Andreasen, S. Gigan, and P. Sebbah, Phys. Rev. Lett. **109**, 033903 (2012).
[57] I. Gozhyk, G. Clavier, R. Méallet-Renault, M. Dvor-

ko, R. Pansu, J.-F. Audibert, A. Brosseau, C. Lafargue, V. Tsvirkun, S. Lozen ko, S. Forget, S. Chénais, C. Ulysse, J. Zyss, and M. Lebental, Phys. Rev. A **86**, 043817 (2012).
[58] H. Bruus and N. D. Whelan, Nonlinearity **9**, 1023 (1996).
[59] E. Bogomolny, N. Pavloff, and C. Schmit, Phys. Rev. E **61**, 3689 (2000).
[60] P. Bellomo and T. Uzer, Phys. Rev. E **50**, 1886 (1994).
[61] H. Primack and U. Smilansky, J. Phys. A **27**, 4439 (1994).
[62] S. Lozenko, N. Djellali, I. Gozhyk, C. Delezoide, J. Lautru, C. Ulysse, J. Zyss, and M. Lebental, J. Appl. Phys **111**, 103116 (2012).
[63] M. Lebental, J. S. Lauret, R. Hierle, and J. Zyss, Appl. Phys. Lett. **88**, 031108 (2006).
[64] Y. F. Chen and K. F. Huang, Phys. Rev. E **68**, 066207 (2003).
[65] G. M. Wysin, J. Opt. A **7**, 502 (2005).
[66] G. M. Wysin, J. Opt. Soc. Am. B **23**, 1586 (2006).
[67] Y.-D. Yang and Y.-Z. Huang, Phys. Rev. A **76**, 023822 (2007).
[68] Y.-D. Yang, Y.-Z. Huang, and S.-J. Wang, IEEE J. Quantum Electron. **45**, 1529 (2009).
[69] S.-J. Wang, Y.-D. Yang, and Y.-Z. Huang, J. Opt. Soc. Am. B **26**, 2449 (2009).
[70] G. Lamé, *Leçons sur la théorie mathématique de l'élasticité des corps solides* (Bachelier, Paris, 1852).
[71] T. Gorin, J. Phys. A **34**, 8281 (2001).
[72] C. Lafargue *et al.*, (unpublished).
[73] S. Åberg, T. Guhr, M. Miski-Oglu, and A. Richter, Phys. Rev. Lett. **100**, 204101 (2008).
[74] B. Dietz, T. Friedrich, M. Miski-Oglu, A. Richter, and F. Schäfer, Phys. Rev. E **78**, 045201 (2008).
[75] R. Dubertrand, E. Bogomolny, N. Djellali, M. Lebental, and C. Schmit, Phys. Rev. A **77**, 013804 (2008).
[76] L. Ge, Q. Song, B. Redding, and H. Cao, Phys. Rev. A **87**, 023833 (2013).